Biological Imaging (2024), 4: e10
doi:10.1017/S2633903X24000138

RESEARCH ARTICLE

Seeing or believing in hyperplexed spatial proteomics via antibodies: New and old biases for an image-based technology

Maddalena M. Bolognesi[1,2], Lorenzo Dall'Olio[3], Amy Maerten[4], Simone Borghesi[5], Gastone Castellani[6] and Giorgio Cattoretti[7]

[1]Istituto di Bioimmagini e Fisiologia Molecolare – CNR, Milan, Italy
[2]National Biodiversity Future Center (NBFC), Palermo, Italy
[3]Laboratorio di Data Science and Bioinformatics, IRCCS Istituto delle Scienze Neurologiche di Bologna – AUSL BO Ospedale Bellaria, Bologna, Italy
[4]Department of in vitro Toxicology and Dermato-Cosmetology, Vrije Universiteit Brussel, Jette, Belgium
[5]Department of Mathematics and Applications, University of Milano Bicocca, Milan, Italy
[6]Department of Experimental, Diagnostic and Specialty Medicine, University of Bologna, Bologna, Italy
[7]Pathology, Department of Medicine and Surgery, Universitá di Milano-Bicocca, Monza, Italy
Corresponding author: Giorgio Cattoretti; Email: giorgio.cattoretti@unimib.it

Received: 13 December 2023; **Revised:** 23 July 2024; **Accepted:** 04 September 2024

Keywords: multiplex staining; dimensionality reduction algorithms; flow cytometry; image analysis; human vision

Abstract

Hyperplexed in-situ targeted proteomics via antibody immunodetection (i.e., >15 markers) is changing how we classify cells and tissues. Differently from other high-dimensional single-cell assays (flow cytometry, single-cell RNA sequencing), the human eye is a necessary component in multiple procedural steps: image segmentation, signal thresholding, antibody validation, and iconographic rendering. Established methods complement the human image evaluation, but may carry undisclosed biases in such a new context, therefore we re-evaluate all the steps in hyperplexed proteomics. We found that the human eye can discriminate less than 64 out of 256 gray levels and has limitations in discriminating luminance levels in conventional histology images. Furthermore, only images containing visible signals are selected and eye-guided digital thresholding separates signal from noise. BRAQUE, a hyperplexed proteomic tool, can extract, in a marker-agnostic fashion, granular information from markers which have a very low signal-to-noise ratio and therefore are not visualized by traditional visual rendering. By analyzing a public human lymph node dataset, we also found unpredicted staining results by validated antibodies, which highlight the need to upgrade the definition of antibody specificity in hyperplexed immunostaining. Spatially hyperplexed methods upgrade and supplant traditional image-based analysis of tissue immunostaining, beyond the human eye contribution.

Impact Statement

Staining with multiple biomarkers in a single tissue section, multiplex staining, is changing how we examine in-situ normalcy, pathology, and the interrelationship of good and bad biological actors. Bioinformatic pipelines developed to deal with high-dimensional datasets such as single-cell RNA sequencing or multiparameter flow cytometry have been adapted to analogous types of data derived from tissue, and co-exist with conventional image analysis tools and human eye-guided image evaluation. We wanted to evaluate if multiplex staining with more than 15 markers (hyperplexed) has comparable sensitivity to conventional image analysis and if these latter analysis tools carry undisclosed biases and should not be used together with hyperplexed staining. We found that the human eye has a reduced discriminative power for grayscale and luminance levels compared to the 8-bit

available spectrum, affecting positive signal recognition above the noise. We also found that the granular analytical power of recent bioinformatic pipelines can extract information from images which defy human eye perception and deliver information unattainable with existing image analysis tools for single-stain images.

1. Introduction

In situ antigen detection in tissues via antibody staining, in transmitted (immunohistochemistry; IHC) or fluorescent light (immunofluorescence; IF) is an established tool in science. It is a space structure preserving assay, complementary to other techniques such as in situ transcriptomics[1] or in situ proteomics.[2] It is also complementing all techniques applied to disaggregated specimens, the latter as single cell suspensions (e.g., single-cell RNA sequencing[3]; scRNAseq) or homogenates.

In recent years, in situ immunostaining has evolved from a single stain (IHC, the staple tool of diagnostic Pathology) to multiple (from two to seven or more) IF stains, to a much higher number of simultaneous co-stains, typically in excess of a dozen, in what is called high-plex or high-dimensional in situ staining or targeted antibody-mediated proteomics.[4] Recommendations for standardization of the diagnostic use of multiplex stains followed,[5] including antibody validation practices.

An analogous progress occurred earlier with flow cytometry (FCM), a technique which employs conjugated antibodies to characterize single-cell suspensions.[6] An acceleration of the evolution of the technique was brought by the use of metal-conjugated antibodies and mass spectrometry for detection (Cytometry by time of flight; CYTOF), in lieu of photodetectors and photomultipliers.[7] The evolution of the technique was accompanied by an evolution of the bioinformatic tools required to handle such an increase in data dimensionality to be analyzed.[8] Most of the bioinformatic tools developed for single-cell assays (scRNAseq, FCM) have been applied to the analysis of single cells in tissue sections.

Low-plex staining (~7–10 biomarkers) is increasingly diffuse, partly owing to the popularity of a signal-enhanced technique (Tyramide Signal Amplification or TSA[9]), however, the image analysis (IA) required for this type of staining does not differ from what is customarily used for single stain images in IHC or IF.[10]

What sets apart hyperplexed in-situ targeted proteomics via antibody immunodetection, the method using high-plex (>15) biomarker determination at cellular or sub-cellular resolution in situ, from other low-plex techniques is the use of bioinformatic tools, proper of other single-cell assays.[11,12] Analogously to FCM and scRNAseq, human visual image assessment is minimal or nil for these processes, despite the ground truth data which are tissue images.

IA tools development[13] has accompanied the production of images all along. Interestingly, one of the main concern of scientists using IA is to identify nuclei in sections,[14] something Surgical Pathologists do effortlessly every day.

IA has been developed not as a replacement for the human eye but as a companion, particularly for simplified one-protein-at-a-time diagnostic immunostains.[15] However multiplex staining data are intrinsically so complex that deep learning-assisted IA has an increasing role in multiple steps, such as image segmentation,[16] data normalization, and cell classification.[17] Yet, the microscope's future evolution in an expert's view still features eyepieces.[18]

We sought to reevaluate the individual components leading to single-cell classification via hyperplexed stains, and in particular the role, when present, of a human visual assessment of images in processes such as assay sensitivity, antibody validation, signal thresholding, and gating and cell segmentation.

By analyzing a public human lymph node dataset with a custom bioinformatic pipeline, BRAQUE,[19] we found that the human eye is dispensable for the analysis of in situ hyperplexed multistainings.

2. Materials and methods

2.1. Ethical background

The study has been approved by the Institutional Review Board Comitato Etico Brianza, N. 3204, "High-dimensional single cell classification of pathology (HDSSCP)," October 2019. Consent was obtained

https://doi.org/10.1017/S2633903X24000138 Published online by Cambridge University Press

from patients who could be contacted or waived according to article 89 of the EU General Data Protection Regulation 2016/679 (GDPR) and decree N. 515, 12/19/2018 of the Italian Privacy Authority.

2.2. Human specimens

Sentinel lymph nodes ($n = 5$) were extracted from the laboratory information systems of the San Gerardo Hospital by the Authors with clinical privileges and anonymized. Paraffin blocks and sections to be analyzed were selected by a Pathologist after a review of the Hematoxylin and Eosin (H&E) stain. Only archival formalin-fixed, paraffin embedded material (FFPE) was used.

2.3. Histology

Chilled paraffin blocks were sectioned in a rotary microtome (Leica Biosystems, Buccinasco, MI, Italy) at 3 μm, sections were placed in a warm waterbath and collected on charged microscope glass slides. After an overnight oven incubation in an upright position, they were further processed for Hematoxylin & Eosin (H&E), IHC, or IF stains.

2.4. Antigen retrieval

Antigen retrieval (AR) was performed by placing the dewaxed, rehydrated sections[20] in a 800 ml glass container filled with the retrieval solutions (EDTA pH 8; 1 mM EDTA in 10 mM Tris-buffer pH 8, Merck Life Science S.r.l., Milano, Italy; cat. T9285), irradiated in a household microwave oven at full speed for 8 min, followed by intermittent electromagnetic radiation to maintain constant boiling for 30 min, and cooling the sections to about 50 °C before use.

2.5. Immunohistochemistry

Primary unconjugated antibodies (Abs) were validated for frozen and for FFPE material according to established criteria[21] (see Supplementary Tables).

For immunohistochemistry (IHC), optimally diluted, validated primary antibodies were applied overnight, washed in 50 mM Tris–HCl buffer (pH 7.5) containing 0.01% Tween-20 (Merck) and 100 mM sucrose (TBS-Ts),[22] counterstained with a horseradish peroxidase–conjugated polymer (Vector Laboratories, Burlingame, CA), washed, developed in DAB (Agilent, Santa Clara, CA), lightly counterstained and mounted.

Serial LN sections were immunostained for the AE1–AE3 pre-made cocktail in a Omnis automated immunostainer (Agilent, Santa Clara, CA) with routine same-day protocols.

2.6. Indirect immunofluorescence

Multiple immunofluorescent (IF) labeling was previously described in detail.[20] Briefly, the sections were incubated overnight with optimally diluted primary antibodies in species or isotype mismatched combinations (e.g., rabbit + mouse, mouse IgG1 + mouse IgG2a), washed and counterstained with specific distinct fluorochrome-tagged secondary antibodies (Supplementary Tables).[20] The slides, counterstained with DAPI and mounted, were scanned on an S60 Hamamatsu scanner (Nikon, Campi Bisenzio, FI, Italy) at 20× magnification. The filter setup for seven color acquisition (DAPI, BV480, FITC, TRITC, Cy5, PerCp, autofluorescence/AF) was as published.[23] Additional data are in the Supplementary Material.

2.7. Tyramide signal amplification

Sections to be processed for TSA were dewaxed, antigen retrieval was performed as mentioned, endogenous peroxidase was blocked, incubated with the primary Ab overnight and processed as per the manufacturer's instruction for Alexa Fluor™ 647 Tyramide (cat. N. B40958; Thermo Fisher

https://doi.org/10.1017/S2633903X24000138 Published online by Cambridge University Press

Scientific, Vedano al Lambro, Italy), a fluorochrome emitting in the red spectrum where tissue autofluorescence is minimal. The Alexa Fluor™ 647 signal was acquired with a 650/13 nm excitation filter, a 694/44 nm emission filter, and a dichroic FF655-Di01 filter[24] and could be combined with other fluorochrome combinations except the ones emitting in the 530–570 nm range, where the TSA-Alexa FluorTM 647 product bleeds. All filters are from Semrock, Lake Forest, Ill. Details of the process can be found in the Supplementary Material.

In the double indirect IF-TSA combined staining, TSA was performed first.

2.8. Preparation of immunofluorescent images for single cell analysis

After the stainings were acquired, digital slide images (.ndpi) were imported as uncompressed .tiff with ImageJ (ImageJ, RRID:SCR_003070). Tissue autofluorescence (AF) was subtracted when appropriate as published.[20]

2.9. Image analysis

IHC/IF staining quantitation: Fluorescence images were imported in Fiji[25] (RRID:SCR_002285). For area quantification, inverted images were adjusted (Brightness/Contrast command) and thresholded (OTSU). The stained area value was normalized for the total nuclear area value (DAPI). For IHC, the image was color deconvoluted[26] and the DAB image was processed as above. Hematoxylin was used for normalization instead of DAPI. Brightness/Contrast, Math transformation (log), and 3D surface plot were used for visualization (see Supplementary Methods).

Two public-domain IA tools were used for nuclear identification: QuPath (RRID:SCR_018257)[27] and CellPose 2.0 (RRID:SCR_021716).[28] Details of the setting for IA are reported in the Supplementary Methods.

Adobe Photoshop 2023 (San Jose, CA) (RRID:SCR_014199) and Adobe Illustrator (RRID:SCR_010279) were used for figure layouts.

2.10. Grayscale tone discrimination test of the human eye

Fourteen pathologists, 11 males and 3 females, aged 43 ± 13.8 years (range 29–71), 14.1 ± 13 years into the profession (range 0–43) were asked to log into the Time magazine website https://time.com/4663496/can-you-actually-see-50-different-shades-of-grey/, perform the test and provide the score obtained. Additional information is provided in the Supplementary Methods section.

2.11. Bit depth reduction discrimination tests

Twelve pathologists with diagnostic digital pathology experience examined a series of continuous gray shaded bars and full-size four-images composites uploaded into NDPserve (Hamamatsu Photonics) via a provided link. The images encompass the various typology of digital images encountered during diagnostic sign-up (Supplementary Figure S1). The bit depth of each image in the composite was changed from the conventional 24 bit (8 bit times three, 256 colors each) to 6, 5, or 4 bit via the Adjustments > Posterize command (Adobe Photoshop 2023), then saved in the new format with the original image size and pixel resolution. The 7-bit image was not used for the histology image test, except for the grayscale gradients bars. The percentage of correct scores for each observer, the image type and bit depth were recorded. Additional information is provided in the Supplementary Methods section.

2.12. High dimensional analysis with BRAQUE

BRAQUE,[19] an acronym for Bayesian Reduction for Amplified Quantization in UMAP Embedding, has been developed for the global analysis of individual cells in tissue sections stained in IF with multiple biomarkers and uses dimensionality reduction algorithms. Is a Python pipeline for automated cluster enhancing, identification, and characterization.

https://doi.org/10.1017/S2633903X24000138 Published online by Cambridge University Press

The key procedure of BRAQUE (whose code may be found on GitHub at https://github.com/LorenzoDallOlio/BRAQUE) consists of a new preprocessing, called lognormal shrinkage. This preprocessing specifically addresses the problem arising from noise due to crossbleed from neighboring cells, in fact, if single-cell data are more distinct and discrete on the other hand spatial proteomics markers assume a more continuous distribution with less clear separation among the modalities.[29,30]

In BRAQUE's preprocessing a mixture of normal distributions is fitted for each of the log-transformed markers, and then each normal component of the mixture is shrunk toward its mean to help further steps counter this continuity and lack of clear separation.

After this crucial step, the markers are standardized and combined in a 2-dimensional latent spaces by the UMAP algorithm. On this embedding space, the clustering of cells is performed by HDBSCAN and lastly, each cluster is tested for significant markers, which are ranked by effect size to help experts with cell type annotation.

The output consists of multiple clusters, whose numerosity is defined by the size of the smallest cluster (usually not below 0.005% of the cell number or ~ 20 cells). Each cluster is defined by (A) markers ranked for probability or possibility to identify the cluster, (B) a tissue map of the cells belonging to the cluster, and (C) the expression of a pre-defined set of diagnostic markers for that cluster, compared to the whole population (Supplementary Figure S1). Each cluster is classified by an expert supervision into cell types.

The HubMap lymph node dataset HBM754.WKLP.262 (doi:10.35079/HBM754.WKLP.262) was downloaded from the HubMap consortium website (https://hubmapconsortium.org/) as a .csv file, thus pre-segmented by the source.

3. Results

3.1. The human eye has a biased vision

In image analysis, the human eye is required to discriminate signal from noise or background.

Published research shows that humans can distinguish about 870 different shades of gray,[31] data which are contradicted by Kreit et al.,[32] who sets the gray level discrimination in humans at about 30 shades.

Fourteen experienced observers produce a gray discrimination score of 37.8 (SD ±4.77) out of 50 (Figure 1) which is below the discrimination of 64 gray tones out of 256 (8-bit scale) (see Supplementary Methods) and in keeping with published results[32] and anecdotal annotations in the public domain (see Supplementary Tables).

The type of images of this test (homogeneously tinted squares surrounded by a thick border) are not the type of images encountered in medicine or biology and may be also prone to hallucinations.[33] We then used microscopy digital images in which the luminance repertoire was reduced from the 256 usual channels (8 bit) down to just 16 (4 bit) (see an example in Figure 2 and Supplementary Figure S3).

While the observers identify laddering (that is reduced bit depth) on the monochrome continuous grayscale images below a mean of 7.7 ± 0.2 bits (range 8–7.5) (Figure 3a and Supplementary Figure S3T), they scored correctly the bit depth of only 51% ± 33% of the images (range 26%–75%). There was no apparent relationship between the ability to identify bit degradation in monochrome bands, which scored at the top for all pathologists, and in histology images (Figure 3a).

The most degraded images (4 bit) were more likely to be correctly identified (Figure 3b). Erroneous bit depth assignment was equivalent in all kinds of common pathology images (Figure 3c), being a single triple immunofluorescent image the most variably scored (mean 35% ± 42% correct score, range 0%–100%) (Figure 3).

The discrimination power for degraded images was highest among the bottom range of bit depth (Figure 3d), with no differences among the image types.

Very detailed images (e.g., colon, testis, LCH) scored marginally better on average than images with low details (brain, muscle, IHC), with 55.8% versus 49.7% correct answers.

https://doi.org/10.1017/S2633903X24000138 Published online by Cambridge University Press

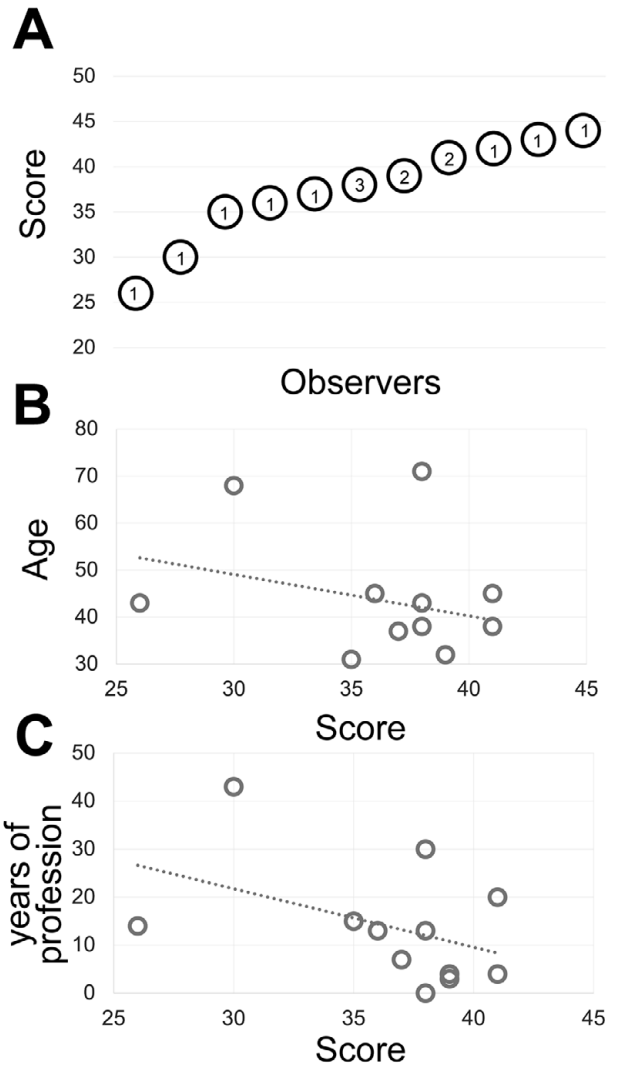

Figure 1. *(a) The shades of gray score distribution of 15 Pathologists, ordered progressively. The number inside each circle is the number of subjects with that score. (b) The relationship between the score (x-axis) and the subject's age (y-axis). The R-squared value of the intercept is* $R^2 = 0.0856$. *(c) The relationship between the score (x-axis) and the pathologist's working experience in years (y-axis). The R-squared value of the intercept is* $R^2 = 0.1876$.

From these experiments, we conclude that the discriminative power of the human eye for details along a 8 bit luminance scale is significantly reduced, compared to the available range.

3.2. Signal enhancement methods may deliver marginal gains

Positive signal brightness affects detection. Thus, we wanted to define the sensitivity of the immunofluorescent techniques used in multiplexing, compared to a brightfield standard, DAB IHC. To do so, we used widely used algorithms for immunostain separation from background and identification such as Otsu and K-mean clustering, which are based on vector quantization. These algorithms do not require tuning and the result reflects the image ground truth according to the gray levels of the image.

https://doi.org/10.1017/S2633903X24000138 Published online by Cambridge University Press

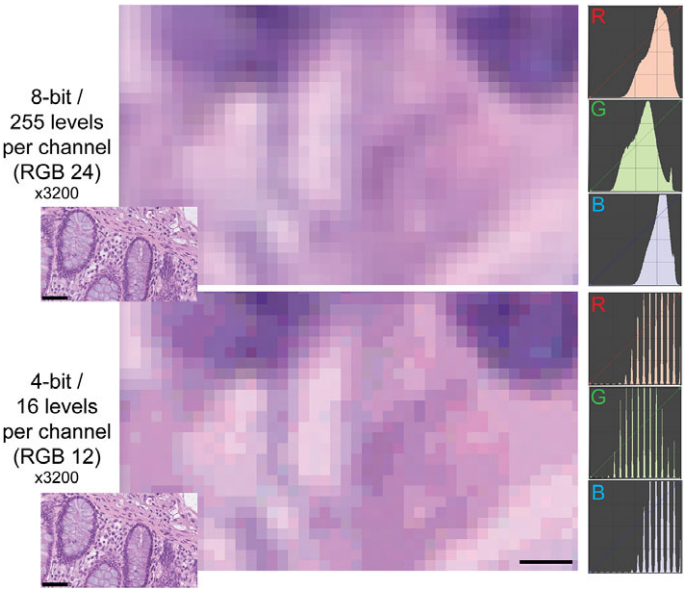

Figure 2. *Example of two different bit depths for an H&E image. The two images represent A, a high magnification detail of an 8 bit (24 bits in RGB) H&E image of the human colon, B the same image at 4 bit depth reduction. The R, G, and B images on the right are the frequency plots of the image pixels, distributed along the 0–255 channels for each of the three color components. Image A contains 255 levels per channel, image B 16 levels, as shown by the laddering of the RGB profile in the RGB details. Note the same size of the visible pixels. Scale bar: 2.25 μm (five pixels; 3200x). The insets in the lower left corner of each image show the full-size originating images (scale bar 50 μm).*

As previously published by others,[34,35] TSA was not superior, compared to DAB, and as good as double indirect IF[20] for some fluorochromes (Figure 4). The use of signal-enhancing methods for immunofluorescent staining may marginally benefit signal detection.

3.3. Simplified image analysis tools lack sensitivity

For quantification, we used images of abundant low molecular keratin 8 and 18 (LMW-KRT) expressed in thin dendrites of fibroblastic reticular cells (FRC), and we found that commonly used thresholding algorithms to quantify IF immunostains fail to account for positive pixels at the low end of the spectrum, despite being visible to the human eye after image rendering (Figure 5).

3.4. Hyperplex staining methods have superior sensitivity

Next, we tested the analytical power of hyperplexed stainings by examining a public human lymph node dataset, composed of 28 antibodies (+ DAPI), for which the segmentation method was previously published.[36] In the panel, a widely used "pan keratin" antibody cocktail, AE1 and AE3[37] was used.

Only AE3 is able to detect KRT8, one of the two LMW-KRT in LN (the other is KRT18). The AE1-AE3 cocktail ("panCK" or "CK") is used daily by thousands of surgical pathologists to detect nodal metastasis from carcinoma. Because a selective epitope condition prevents the broad detection of LN FRC with this cocktail, only occasional KRT8+ cells are being detected.[38] The presence of a panCK reagent in the dataset made a comparison of the detection power possible between single-stains and hyperplexed images, by enumerating the positive cell types.

https://doi.org/10.1017/S2633903X24000138 Published online by Cambridge University Press

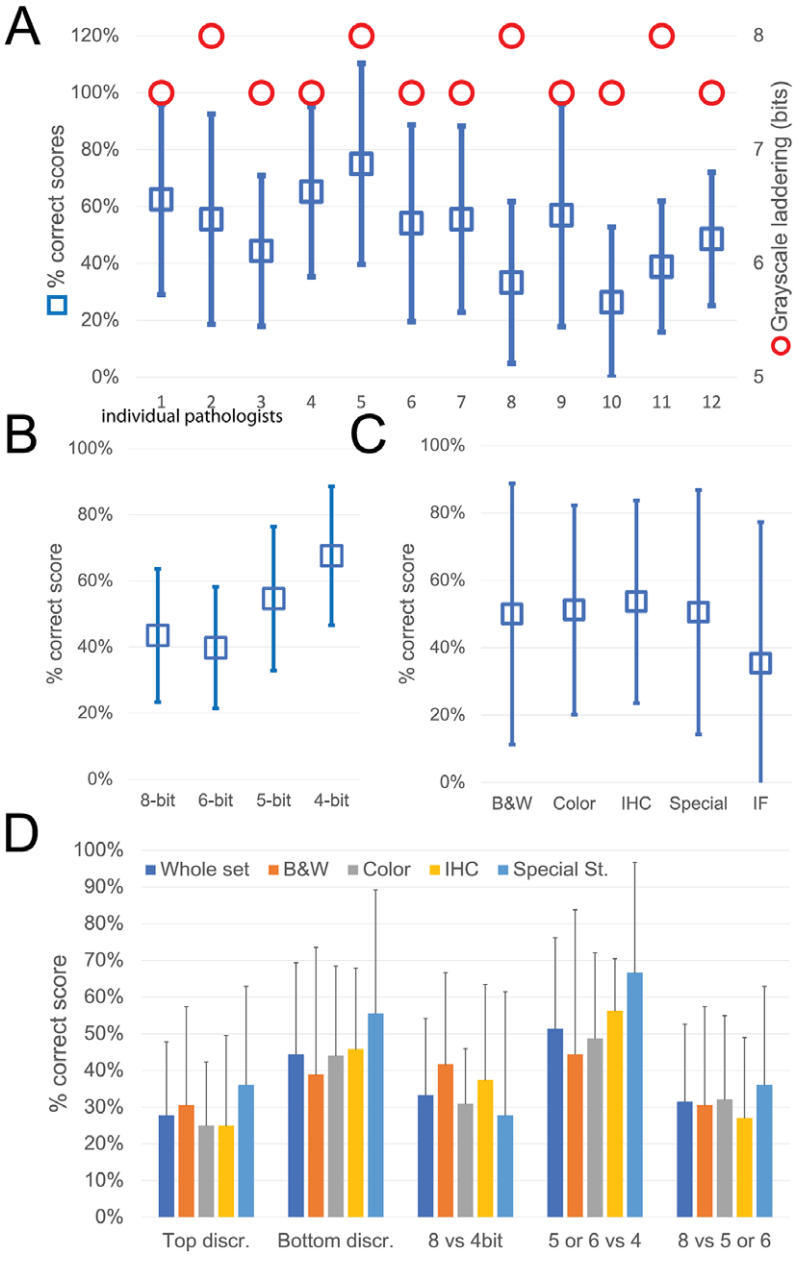

Figure 3. *Descriptive graphics of the bit-reduced images scores. (a) The two-scale image shows the bit depth below which each of the 12 pathologists identifies degradation on a monochrome image (red circles; scale to the right). The mean ± SD percentage of correct bit depth identification on the global test is shown (blue squares; scale to the left). (b) Mean percentage ± SD of correct identification on images divided by bit depth. (c) Mean percentage ± SD of correct identification on images divided by image type. B&W: grayscale images; Color: H&E-stained images; IHC: immunohistochemistry examples; Special: special stains; IF: immunofluorescence. (d) Mean percentage ± SD of correct bit depth identification subdivided between top discrimination (discrimination between 8 and 6 bits), bottom discrimination (5 and 4 bits), 8 bits versus 4 bits, 5 or 6 bits versus 4 bits, 8 bits versus 5 or 6 bits. The scores are further shown for the whole test or divided by image type (B&W: grayscale images; Color: H&E-stained images; IHC: immunohistochemistry examples; Special: special stains).*

https://doi.org/10.1017/S2633903X24000138 Published online by Cambridge University Press

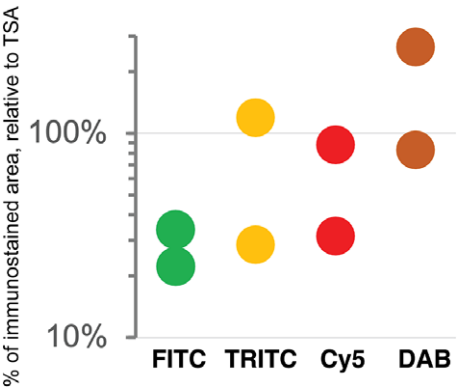

Figure 4. *Comparison of sensitivity of detection systems. The area of detection of anti-LMW KRT in serial LN section by secondary Abs conjugated with three fluorochromes (FITC = Alexa 488 green, TRITC = Rhodamine Red™ X orange, Cy5 = Alexa 647 red) and DAB is plotted on a logarithmic scale, relative to the area detected with TSA Alexa 647 (100%). Duplicate experiments.*

We applied to the HubMap dataset BRAQUE,[19] a dimensionality reduction algorithms-based analytical pipeline (DRAAP) designed for the spatial Ab-based proteomic data in multiplex, which do not requires pre-definition of positive signal thresholds.

BRAQUE was able to identify 12 clusters containing CK+ cells for a total of 16,698 cells out of 188,450 (9.24%) (Table 1, Supplementary Tables, and Supplementary Figures S1 and S2).

Nine clusters expressed SMA together with CK, a known phenotype of FRC,[39] together with variable expression of CollagenIV, CD35 and Podoplanin. These cells accounted for 7.54% of the LN population (13,621 cells).

Three clusters (3,077 cells, 1.70%) had an endothelial phenotype (CD34+ CD31+), where the CK signal could be bleeding from adjacent FRC. A total of 8,196 cells (4.54%) had a stromal phenotype devoid of CK, divided into fibroblasts (4.30%) and SMA-expressing myofibroblasts (0.23%). The tissue distribution of CK+ FRC and fibroblasts is partially overlapping and distinct from endothelial cells (Figure 6).

A distinct population of Lyve1+ sinus lining cells coexpressed CD31, Vimentin, CD107a but not CD34 (Supplementary Figure S4).

None of these stromal clusters expressed CD44, CD45, or CD45RO, or any other leukocyte-restricted marker. The complete cell classification results are available in the Supplementary Methods (Supplementary Tables).

The spatial distribution of the FRC clusters is consistent with the known tissue location and the percentage of total stromal cells (Table 1).

7.4% of the segmented cells were contained in nine clusters which could not be classified (unclear, artifacts) in addition to cells discarded by BRAQUE (6.8%) upfront on a statistical basis.

By analyzing the same dataset with Phenograph, a similar classification was obtained, including the identification of CK+ stromal cell clusters (Supplementary Figure S5).

To estimate how the percentage of CK+ FRC detected by BRAQUE in the single HubMap LN would position among the results obtained with an available single-stain, single-cell quantitative tool, QuPath, we quantified the IHC stain of two different antibody cocktails: the AE1–AE3 mixture and a two-rabbit monoclonal antibodies cocktail directed at low molecular weight keratin 8–18. AE1–AE3 labeled 9.27% ± 6.79% cells (5 sentinel LN), the LMW keratin cocktail 8.05% ± 7.02% (4 sentinel LN). We also used QuPath to quantify the IF stains used for the TSA and the control experiments. Quantification of IF stains in QuPath was highly erratic because of the difficulty of discriminating by eye signal from autofluorescent background (see Supplementary Tables).

https://doi.org/10.1017/S2633903X24000138 Published online by Cambridge University Press

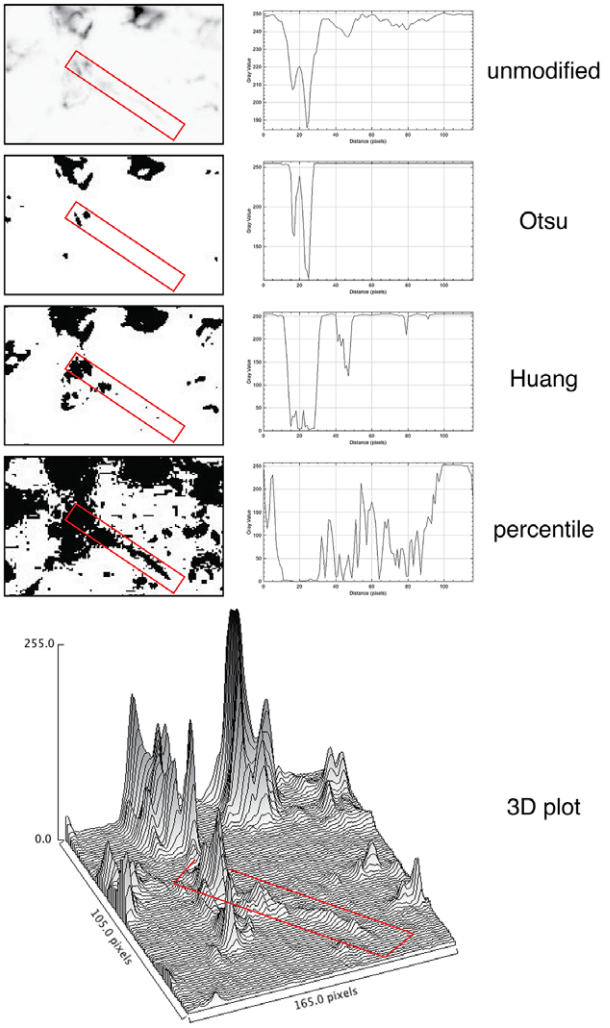

Figure 5. *Thresholding LMW KRT staining in LN. The LMW KRT IF stain detail is shown as an inverted, unmodified image, modified with three different Fiji thresholding algorithms (Otsu, Huang, and percentile) and as a 3D plot. Only three thresholding algorithms are shown, out of 17 tested. A FRC CK+ dendrite is highlighted with a red rectangle and the mean pixel density value along that rectangle is shown next to the image. Note that, because of the image inversion, darker pixels have lower values in the plot. The continuous intensity variations of the signal above background can be appreciated in the 3D plots. Note that the percentile algorithm highlights numerous background spots in addition to the dendrite of interest. The image shown measures 105 × 165 pixels (47.5 × 74.25 μm).*

3.5. Hyperplexed staining methods can handle images unreadable by the human eye

We obtained the raw IF images from the HubMap dataset and we could not visualize a distinct CK+ cell population except by applying an image log transformation combined with virtual 3D visualization, after which we were able to identify a weak CK signal co-localizing with vimentin and SM actin (Figure 7a and Supplementary Figure S6).

Since additional sections from the CODEX LN sample were not available, we used in-house processed FFPE LN sections and stained them with an aliquot of the original AE3 antibody, which we found still effective on a positive control after 37 years[40] (Supplementary Figure S7).

https://doi.org/10.1017/S2633903X24000138 Published online by Cambridge University Press

Table 1. *Stromal cells and phenotypes*

BRAQUE cell classification	Clusters	Total cells	%	% of total	Typical phenotype
CK+ FRC	9	13621	32.17	7.54	SMA, CK, CD35, CollIV, PDPN, VIM
Fibroblasts	5	7776	18.37	4.30	VIM, CollIV, PDPN
Myofibroblasts	3	420	0.99	0.23	CD34, SMA, CollIV
Endothelium (CK+)	3	3077	7.27	1.70	CD34, CD31, VIM, CK
Endothelium	10	7021	16.58	3.89	CD31, CD34, CollIV, VIM,
Lyve1+ endothelium	8	8755	20.68	4.84	Lyve1, CD107a, CD31
FDC	2	1671	3.95	0.92	CD21, PDPN, CD35, CD20
Total stromal cells	38	42341	100.0	23.43	
Total cells	90	180708		100.0	

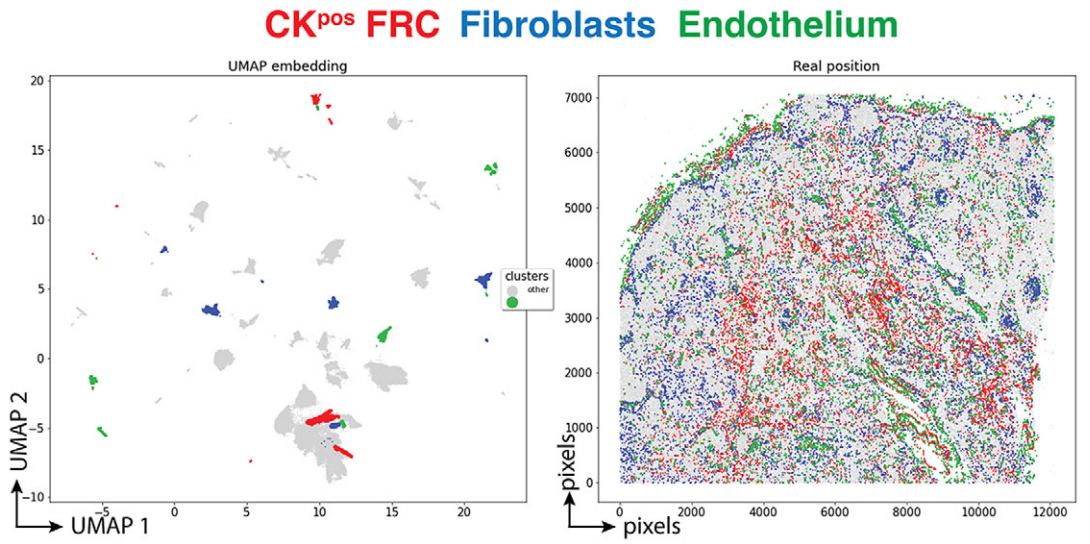

Figure 6. *Tissue distribution of FRC and stromal cells. The distribution of CK+ FRC (red; clusters 3, 6, 12, 22, 23, 56, 60, 78, 87), fibroblasts & myofibroblasts (blue; clusters 24, 31, 32, 36, 54, 59, 73, 82) and endothelial cells (green; clusters 13, 14, 17, 25, 28, 29, 37, 46, 53, 72) is shown plotted on the UMAP plot (left) and on a gray image of the LN section (right). The x and y scales on the left are UMAP virtual space arbitrary references, on the right real pixel image dimensions (0.45 μm per pixel). The gray outlines represent the remaining cell clusters (left) and the total of single cells (right).*

By optimizing the staining conditions[41] and enhancing the image contrast, numerous AE3+ cells co-localize with a LMW KRT staining (Figure 7c), in addition to other stained cells. The latter appeared to be B cells, based on location and aggregation (no B cell markers were co-stained). TSA amplification of the AE3 signal did not improve the stain (Supplementary Figures S8 and S9).

The staining pattern of in-house CK staining of the lymph node reproduced what was obtained from the CODEX dataset, including the follicular B cell staining (Figure 7b).

https://doi.org/10.1017/S2633903X24000138 Published online by Cambridge University Press

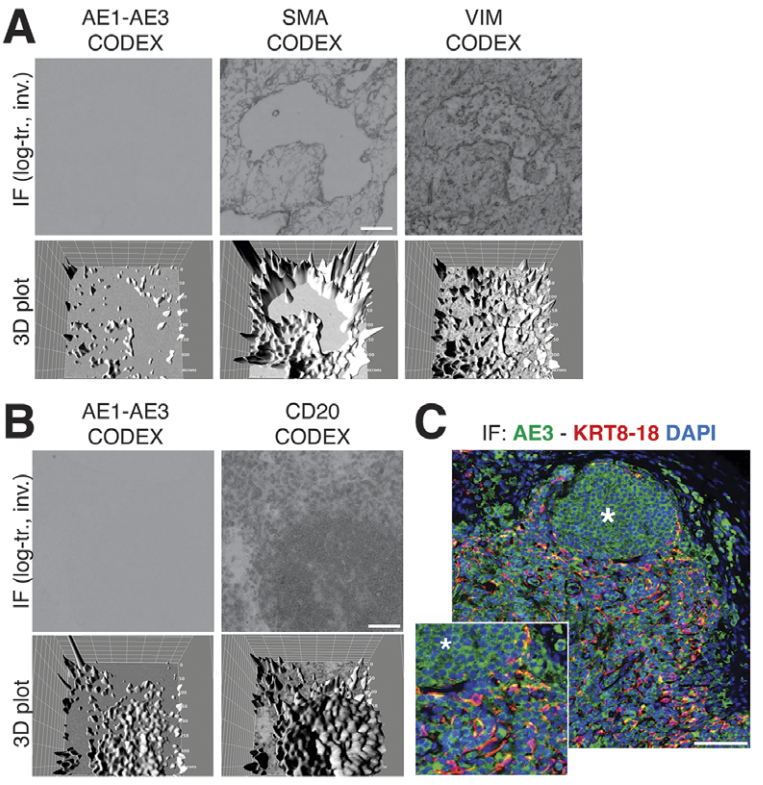

Figure 7. *Image rendering of CK+ FRC. (a) A detail of three markers, CK AE1–AE3, Vimentin and SMA as 2D log-transformed and inverted fluorescence CODEX images (top row) and the 3D transformation of each (bottom row), is shown. (b) The same type of images are shown for another tissue detail, comparing CK AE1-AE3 and a B cell marker, CD20. Scale bar: 100 μm. (c) A low and a high power magnification detail show a three-color image of a LN, produced in-house, where nuclei are blue (DAPI) CK AE3 is green and a LMW KRT cocktail is red. In this image, note a B cell follicle (asterisk) and coexpression of AE3 and LMW KRT in FRC as yellow (green + red). Scale bar: 100 μm.*

4. Discussion

The upper discrimination limit of 64 shades of gray we have shown implies that in the best scenario, signals 4 gray intensity levels (at 8 bit) brighter than noise (256 divided by 64) cannot be discriminated against by the human eye, in addition to known visual and cognitive traps.[33] We thus confirm published data[32] and a number of publicly available anecdotal observations (see Supplementary Tables).

Lack of discrimination of signal from noise broadly affects the appreciation of the full spectrum of biomarker distribution, both in light microscopy and IF. Despite having at disposal the most sensitive stain, IHC with DAB, IA tools are based on algorithms which do not reliably account for signals at the low end of the spectrum. In IHC and IF, a dichotomous image representation (pos/neg) after thresholding is the rule, because of the human eye limit.

Manual gating (i.e., the application of a threshold/barrier discriminating two sets of variables) is considered the main source of data variability and inconsistency in FCM,[8,42,43] but has never been addressed in tissue staining. The lack of awareness of this limit, results in most of the high-dimensional approach to in-situ cell classification to take advantage of a gating strategy at some point during the process.[29,44–47]

https://doi.org/10.1017/S2633903X24000138 Published online by Cambridge University Press

Establishing a signal threshold has three effects, not all negative: *i)* positively assigning a cell to a lineage, *ii)* removing "unwanted" evidence, and *iii)* limiting the discovery of new cell types, based on novel phenotypic profiles.

In hyperplexed staining, the limitation in the number of Abs which can fit in a spatial panel forces the selection of biomarkers with *i)* high "diagnostic" value, *ii)* dichotomic expression, and *iii)* little overlap with other markers in the panel. A gating strategy to cluster classification[29,47] is a consequence.

This sparing choice results in a deductive approach to the cell classification, which is not ideal to discover new cell types[44] and prone to overlook unexpected reactivities.

The selection and validation of the antibodies for in-situ staining[48] are made in general either in unrelated substrates (cell extracts, FCM, tumor clonal proliferations) or in tissue staining devoid of phenotypic detail, mostly derived by single color IHC (see Supplementary Data S1[47] as an example). Strong staining by visual inspection is favored while concurrent additional weak tissue reactivity is ignored and cataloged as "background."

Dimensionality reduction algorithms-based analytical pipelines (DRAAPs) extract from spatial images granular data which cannot be acquired by human eye-guided visual representation nor by manual signal thresholding. Both Phenograph and BRAQUE sample the whole range of pixel values, with the difference that BRAQUE provides a phenotypic profile for each cluster, which is based on statistically ranked characterizing markers, chosen from the whole biomarker set, agnostic of the cell type definition meaning and not relying on preset thresholds. The roster of cluster-defining markers includes expected diagnostic Abs, but also unexpected novel expressions such as CD35 and podoplanin (PDPN) on FRC and CD107a/LAMP1 on sinus lining Live1+ endothelial cells. The advantage of BRAQUE and FlowSOM[49] is to provide marker-agnostic cluster-by-cluster evaluation of the key markers statistical relevance (BRAQUE) or mean marker intensity ("star charts"; FlowSOM), and to present the evidence to human judgment.

BRAQUE introduces an innovative data pre-processing step, Lognormal Shrinkage, which is able to enhance input fragmentation by fitting a lognormal mixture model and shrink each component toward its median.[19] It is therefore able to further subdivide signals in the low range and feed these discretized values to the DRAAP. The final effect is somewhat analogous to the introduction of the "logicle" module for FCM.[6]

As a result, BRAQUE is ranking AE3 levels in FRC and in those cells only in the significant first or second tiers (see Supplementary Tables) despite the very low levels. In other words, BRAQUE provides statistical strength to the visual perception in Figure 7c that AE3 and LMW KRT are co-expressed, thus validated according to the "differential antibody" validation criteria,[21,50] but in those cells only. Worth noting that BRAQUE allocates the CK signal in B cells only and not in other hematolymphoid cells (Supplementary Data), and in the lowest tier when significant.

Notably, there is another antibody which unexpectedly shows up in FRC: CD35 (Supplementary Tables and Supplementary Figure S4). CR1 (the protein name of CD35) is not listed in the Human Protein Atlas (https://www.proteinatlas.org) to be expressed in fibroblasts and in LN, only in the follicular dendritic cells, B cells and macrophages.

CD107a (LAMP1) is listed by the Human Protein Atlas as ubiquitous, however, according to BRAQUE, is differentially expressed only in Lyve1+ endothelial cells and some types of macrophages. These data would not be anticipated by a traditional imaging (Supplementary Tables and Supplementary Figure S4) or image analysis. Interestingly, BRAQUE do not list LAMP1 among the ranked markers in neutrophils (Supplementary Data), because the mean expression in these cells falls within the average variation of the rest of the cells.

Our experience from ongoing research (manuscript in preparation) is that the analytical power of DRAAPs and of BRAQUE in particular will discover quite a few other examples of "validated" antibodies which need to be reassessed because of single cell classification. This may be due to inadequate validation upfront however we favor the hypothesis of missed low-level expression during antibody characterization.

The shortcomings of a visual-guided appreciation of in situ immune detection are numerous.

https://doi.org/10.1017/S2633903X24000138 Published online by Cambridge University Press

There are published data showing the expression of certain biomarkers which have never been reproduced by in situ staining; one example is CD5, shown by RNA and protein on conventional dendritic cells type 2 (cDC2) by high dimensional analysis[51–57] but not on tissue with in situ IF (Wood et al.[58] and manuscript in preparation). Another example is AID, the enzyme required in the nucleus to perform DNA alterations, which for some time has been detected only in the cytoplasm[59] and still not detected[60] in the presence of the RNA message.[61]

Notices about the limitation of an eye-guided approach in high-dimensional studies have just begun to appear in the specialized literature.[62,63]

DRAAPs sensitivity is superior to IA tools used in a conventional setting of low-plex staining. However, saying that DRAAPs are more sensitive is an oversimplification, which blurs the details of how this result is acquired.

First, the algorithm computes the mean expression of all markers in a given cell against all others. Most importantly, data are analyzed as continuous variables, as for FCM,[64] because they use normalized mean signal intensity data from single cells, despite the fact that biomarkers may be selected for all-or-nothing expression.

Second, there must be enough biomarkers in the panel in order to classify as different cells which would otherwise be clustered together. Note that DRAAPs can identify cells not only based on present, but also on absent markers.[65]

Third, the algorithm must be robust enough not to be disturbed by noise.[29]

Fourth, unlike Principal Component Analysis (PCA) which requires at least 2 dimensions, other DRAAPs do not have a minimum number of dimensions to identify meaningful relationships among the data; however, the higher the number of dimensions/parameters provided, the better the discriminative power.

And as a word of caution, fifth, DRAAPs work in a relative space run by mathematics, and can score segmented cells as "negative" for a given biomarker, because statistically below a "mean average" or not above the noise level; in some cases the mean average signal may be considered "positive" by human visual evaluation.

In case the markers are not gated in advance, the product of the DRAAPs is a probabilistic phenotype, because of the inner mathematical working of the algorithm. To go from there to a cell-type cluster classification, other steps are required: deep learning cell classification[66] and/or human intervention, neither envisioning visual appreciation of images.

In conclusion, it is about time for hyperplexed spatial proteomics to reduce the dependency from multicolor IF images and the biases associated with human vision and to embrace a space savvy bioinformatic approach like the one that FCM and scRNAseq currently employ. The huge bonus of relinquishing visual imaging and gating is the ability to discover new cell types and cell functions,[66] at the cost of revisiting the significance and specificity of the biomarkers which identify such novel populations.

Abbreviations

Ab	antibody
BRAQUE	Bayesian Reduction for Amplified Quantization in UMAP Embedding
CK	cytokeratin
CYTOF	cytometry by time of flight
DAB	diaminobenzidine
DRAAP	dimensionality reduction algorithms-based analytical pipeline
FCM	flow cytometry
FDC	follicular dendritic cells
FFPE	formalin-fixed, paraffin-embedded
FRC	fibroblastic reticular cells
IA	image analysis

https://doi.org/10.1017/S2633903X24000138 Published online by Cambridge University Press

IHC	immunohistochemistry
IF	immunofluorescence
IHC	immunohistochemistry
LMW-KRT	low molecular weight keratins
MILAN	Multiple Iterative Labeling by Antibody Neodeposition
scRNAseq	single cell RNA sequencing
TSA	tyramide signal amplification

Supplementary material. The supplementary material for this article can be found at http://doi.org/10.1017/S2633903X24000138.

Data availability statement. The human LN dataset belongs to The Human Body at Cellular Resolution: the NIH Human BioMolecular Atlas Program (doi:10.1038/s41586-019-1629-x). The results here are in whole or part based upon data generated by the NIH Human BioMolecular Atlas Program (HuBMAP): https://hubmapconsortium.org. The image files and the .csv file for a human LN immunostained with the CODEX platform (now PhenoCycler, Akoya Biosciences, Delaware) are accessed at the HubMap website (https://portal.hubmapconsortium.org/), and for the sample HBM754.WKLP.262 (doi:10.35079/HBM754.WKLP.262) at https://portal.hubmapconsortium.org/browse/dataset/c95d9373d698faf60a66ffdc27499fe1 (last accessed June 11, 2023).

Additional data (the clusters definition produced with BRAQUE, .ndpi IF images, the images for the bit reduction test, etc.) are deposited in Bicocca Open Archive Research Data (BOARD).Bolognesi, Maddalena; Dall'Olio, Lorenzo; Maerten, Amy; Borghesi, Simone; Castellani, Gastone; Cattoretti, Giorgio (2023), "Seeing or believing in hyperplexed spatial proteomics via antibodies.", Bicocca Open Archive Research Data, V1, doi: 10.17632/kmxz7fgydx https://data.mendeley.com/datasets/kmxz7fgydx/1

Acknowledgments. We wish to thank Christopher Wilson (Time Inc., New York) for sharing the code of the website used for testing, Mario R. Faretta (IEO, Milan, Italy) for invaluable advice, and the Pathologists who contributed suggestions and human visual scoring of synthetic and real-life tests, Elisa Belloni, Francesca M. Bosisio, Alessandro Caputo, Giorgio Cazzaniga, Roberta Ciccimarra, Vincenzo L'Imperio, Fabio Pagni, Davide Seminati, Claudio Tripodo, and Matteo Zoboli.

Author contribution. L.D., S.B., and G.Cast. generated BRAQUE. G.Cat. and A.M. performed immunostains. M.M.B., G.Cat., and L.D. analyzed the data. G.Cat. and G.Cast. wrote the manuscript. M.M.B. and L.D. contributed equally to this work.

Funding statement. G.Cat. and M.M.B. received funding from Regione Lombardia POR FESR 2014–2020, Call HUB Ricerca ed Innovazione: ImmunHUB. G.Cast. received funding from the EU Horizon 2020 programme (GenoMed4All project #101017549, HARMONY and HARMONY-PLUS project #116026), and the AIRC Foundation (Associazione Italiana per la Ricerca contro il Cancro; Milan, Italy; projects #26216).

Competing interest. The authors declare none.

Reference

1. Le P, Ahmed N, Yeo GW. Illuminating RNA biology through imaging. *Nature Cell Biology.* 2022;**24**(6):815– 24.
2. Mund A, Coscia F, Kriston A, Hollandi R, Kovács F, Brunner A-D, Migh E, Schweizer L, Santos A, Bzorek M, Naimy S, Rahbek-Gjerdrum LM, Dyring-Andersen B, Bulkescher J, Lukas C, Eckert MA, Lengyel E, Gnann C, Lundberg E, Horvath P, Mann M. Deep Visual Proteomics defines single-cell identity and heterogeneity. *Nature Biotechnology.* 2022;**40**(8):1231–40.
3. Svensson V, Vento-Tormo R, Teichmann SA. Exponential scaling of single-cell RNA-seq in the past decade. *Nat Protoc.* 2018;**13**(4):599–604.
4. De Smet F, Antoranz Martinez A, Bosisio FM. Next-Generation Pathology by Multiplexed Immunohistochemistry. *Trends in Biochemical Sciences.* 2021;**46**(1):80–2.
5. Taube JM, Akturk G, Angelo M, Engle EL, Gnjatic S, Greenbaum S, Greenwald NF, Hedvat CV, Hollmann TJ, Juco J, Parra ER, Rebelatto MC, Rimm DL, Rodriguez-Canales J, Schalper KA, Stack EC, Ferreira CS, Korski K, Lako A, Rodig SJ, Schenck E, Steele KE, Surace MJ, Tetzlaff MT, von Loga K, Wistuba II, Bifulco CB, Society for Immunotherapy of Cancer Pathology Task F. The Society for Immunotherapy of Cancer statement on best practices for multiplex immunohistochemistry (IHC) and immunofluorescence (IF) staining and validation. *J Immunother Cancer.* 2020;**8**(1).
6. Herzenberg LA, Tung J, Moore WA, Herzenberg LA, Parks DR. Interpreting flow cytometry data: a guide for the perplexed. *Nature Immunology.* 2006;**7**(7):681–5.
7. Olsen LR, Leipold MD, Pedersen CB, Maecker HT. The anatomy of single cell mass cytometry data. *Cytometry A.* 2019;**95**(2):156–72.

8. Mair F, Hartmann FJ, Mrdjen D, Tosevski V, Krieg C, Becher B. The end of gating? An introduction to automated analysis of high dimensional cytometry data. *European Journal of Immunology.* 2016;**46**(1):34–43.
9. van Gijlswijk RP, Zijlmans HJ, Wiegant J, Bobrow MN, Erickson TJ, Adler KE, Tanke HJ, Raap AK. Fluorochrome-labeled tyramides: use in immunocytochemistry and fluorescence in situ hybridization. *J Histochem Cytochem.* 1997;**45**(3):375–82.
10. Aeffner F, Zarella MD, Buchbinder N, Bui MM, Goodman MR, Hartman DJ, Lujan GM, Molani MA, Parwani AV, Lillard K, Turner OC, Vemuri VNP, Yuil-Valdes AG, Bowman D. Introduction to Digital Image Analysis in Whole-slide Imaging: A White Paper from the Digital Pathology Association. *J Pathol Inform.* 2019;**10**:9.
11. Clarke ZA, Andrews TS, Atif J, Pouyabahar D, Innes BT, MacParland SA, Bader GD. Tutorial: guidelines for annotating single-cell transcriptomic maps using automated and manual methods. *Nature Protocols.* 2021;**16**(6):2749–64.
12. Heumos L, Schaar AC, Lance C, Litinetskaya A, Drost F, Zappia L, Lucken MD, Strobl DC, Henao J, Curion F, Single-cell Best Practices C, Schiller HB, Theis FJ. Best practices for single-cell analysis across modalities. *Nat Rev Genet.* 2023;**24**(8): 550–72.
13. Ljosa V, Carpenter AE. Introduction to the quantitative analysis of two-dimensional fluorescence microscopy images for cell-based screening. *PLoS computational biology.* 2009;**5**(12):e1000603.
14. Jamali N, Dobson ET, Eliceiri KW, Carpenter AE, Cimini BA. BioImage Analysis Survey: Community experiences and needs for the future. *Biol Imaging.* 2022;**1**.
15. Czerniak B, Herz F, Wersto RP, Alster P, Puszkin E, Schwarz E, Koss LG. Quantitation of oncogene products by computer-assisted image analysis and flow cytometry. *J Histochem Cytochem.* 1990;**38**(4):463–6.
16. Ma J, Wang B. Towards foundation models of biological image segmentation. *Nature Methods.* 2023;**20**(7):953–5.
17. Amitay Y, Bussi Y, Feinstein B, Bagon S, Milo I, Keren L. CellSighter: a neural network to classify cells in highly multiplexed images. *Nat Commun.* 2023;**14**(1):4302.
18. Carpenter AE, Cimini BA, Eliceiri KW. Smart microscopes of the future. *Nat Methods.* 2023;**20**(7):962–4.
19. Dall'Olio L, Bolognesi M, Borghesi S, Cattoretti G, Castellani G. BRAQUE: Bayesian Reduction for Amplified Quantization in UMAP Embedding. *Entropy (Basel).* 2023;**25**(2).
20. Bolognesi MM, Manzoni M, Scalia CR, Zannella S, Bosisio FM, Faretta M, Cattoretti G. Multiplex Staining by Sequential Immunostaining and Antibody Removal on Routine Tissue Sections. *J Histochem Cytochem.* 2017;**65**(8):431–44.
21. Bolognesi MM, Mascadri F, Furia L, Faretta M, Bosisio FM, Cattoretti G. Antibodies validated for routinely processed tissues stain frozen sections unpredictably. *Biotechniques.* 2021;**70**(3):137–48.
22. Cattoretti G, Bosisio F, Marcelis L, Bolognesi MM. Multiple Iterative Labeling by Antibody Neodeposition (MILAN): Nature Research; 2019 [updated September 25, 2019. Available from: https://protocolexchange.researchsquare.com/article/nprot-7017/v5.
23. Mascadri F, Ciccimarra R, Bolognesi MM, Stellari F, Ravanetti F, Cattoretti G. Background-free Detection of Mouse Antibodies on Mouse Tissue by Anti-isotype Secondary Antibodies. *J Histochem Cytochem.* 2021;**69**(8):535–41.
24. Mascadri F, Bolognesi MM, Pilla D, Cattoretti G. Rejuvenated Vintage Tissue Sections Highlight Individual Antigen Fate During Processing and Long-term Storage. *J Histochem Cytochem.* 2021;**69**(10):659–67.
25. Schindelin J, Arganda-Carreras I, Frise E, Kaynig V, Longair M, Pietzsch T, Preibisch S, Rueden C, Saalfeld S, Schmid B, Tinevez J-Y, White DJ, Hartenstein V, Eliceiri K, Tomancak P, Cardona A. Fiji: an open-source platform for biological-image analysis. *Nature methods.* 2012;**9**(7):676–82.
26. Ruifrok AC, Johnston DA. Quantification of histochemical staining by color deconvolution. *Anal Quant Cytol Histol.* 2001;**23** (4):291–9.
27. Bankhead P, Loughrey MB, Fernandez JA, Dombrowski Y, McArt DG, Dunne PD, McQuaid S, Gray RT, Murray LJ, Coleman HG, James JA, Salto-Tellez M, Hamilton PW. QuPath: Open source software for digital pathology image analysis. *Scientific reports.* 2017;**7**(1):16878.
28. Pachitariu M, Stringer C. Cellpose 2.0: how to train your own model. *Nature methods.* 2022;**19**(12):1634–41.
29. Hickey JW, Tan Y, Nolan GP, Goltsev Y. Strategies for Accurate Cell Type Identification in CODEX Multiplexed Imaging Data. *Front Immunol.* 2021;**12**:727626.
30. Zhang W, Li I, Reticker-Flynn NE, Good Z, Chang S, Samusik N, Saumyaa S, Li Y, Zhou X, Liang R, Kong CS, Le Q-T, Gentles AJ, Sunwoo JB, Nolan GP, Engleman EG, Plevritis SK. Identification of cell types in multiplexed in situ images by combining protein expression and spatial information using CELESTA. *Nature methods.* 2022;**19**(6):759–69.
31. Kimpe T, Tuytschaever T. Increasing the number of gray shades in medical display systems–how much is enough? *Journal of digital imaging.* 2007;**20**(4):422–32.
32. Kreit E, Mäthger LM, Hanlon RT, Dennis PB, Naik RR, Forsythe E, Heikenfeld J. Biological versus electronic adaptive coloration: how can one inform the other? *Journal of the Royal Society, Interface.* 2013;**10**(78):20120601.
33. Aeffner F, Wilson K, Martin NT, Black JC, Hendriks CLL, Bolon B, Rudmann DG, Gianani R, Koegler SR, Krueger J, Young GD. The Gold Standard Paradox in Digital Image Analysis: Manual Versus Automated Scoring as Ground Truth. *Arch Pathol Lab Med.* 2017;**141**(9):1267–75.
34. Hötzel KJ, Havnar CA, Ngu HV, Rost S, Liu SD, Rangell LK, Peale FV. Synthetic Antigen Gels as Practical Controls for Standardized and Quantitative Immunohistochemistry. *Journal of Histochemistry & Cytochemistry.* 2019;**67**(5):309–34.
35. Berry S, Giraldo NA, Green BF, Cottrell TR, Stein JE, Engle EL, Xu H, Ogurtsova A, Roberts C, Wang D, Nguyen P, Zhu Q, Soto-Diaz S, Loyola J, Sander IB, Wong PF, Jessel S, Doyle J, Signer D, Wilton R, Roskes JS, Eminizer M, Park S, Sunshine JC, Jaffee EM, Baras A, De Marzo AM, Topalian SL, Kluger H, Cope L, Lipson EJ, Danilova L, Anders RA, Rimm DL,

https://doi.org/10.1017/S2633903X24000138 Published online by Cambridge University Press

Pardoll DM, Szalay AS, Taube JM. Analysis of multispectral imaging with the AstroPath platform informs efficacy of PD-1 blockade. *Science.* 2021;**372**(6547).

36. Kennedy-Darling J, Bhate SS, Hickey JW, Black S, Barlow GL, Vazquez G, Venkataraaman VG, Samusik N, Goltsev Y, Schürch CM, Nolan GP. Highly multiplexed tissue imaging using repeated oligonucleotide exchange reaction. *European Journal of Immunology.* 2021;**51**(5):1262–77.
37. Woodcock-Mitchell J, Eichner R, Nelson WG, Sun TT. Immunolocalization of keratin polypeptides in human epidermis using monoclonal antibodies. *J Cell Biol.* 1982;**95**(2 Pt 1):580–8.
38. Linden MD, Zarbo RJ. Cytokeratin immunostaining patterns of benign, reactive lymph nodes: applications for the evaluation of sentinel lymph node specimen. *Applied Immunohistochemistry & Molecular Morphology.* 2001;**9**(4):297–301.
39. Franke WW, Moll R. Cytoskeletal components of lymphoid organs. I. Synthesis of cytokeratins 8 and 18 and desmin in subpopulations of extrafollicular reticulum cells of human lymph nodes, tonsils, and spleen. *Differentiation.* 1987;**36**(2):145–63.
40. Argentieri MC, Pilla D, Vanzati A, Lonardi S, Facchetti F, Doglioni C, Parravicini C, Cattoretti G. Antibodies are forever: a study using 12-26-year-old expired antibodies. *Histopathology.* 2013;**63**(6):869–76.
41. Furia L, Pelicci S, Perillo F, Bolognesi MM, Pelicci PG, Facciotti F, Cattoretti G, Faretta M. Automated multimodal fluorescence microscopy for hyperplex spatial-proteomics: Coupling microfluidic-based immunofluorescence to high resolution, high sensitivity, three-dimensional analysis of histological slides. *Front Oncol.* 2022;**12**:960734.
42. Saeys Y, Van Gassen S, Lambrecht BN. Computational flow cytometry: helping to make sense of high-dimensional immunology data. *Nature Reviews Immunology.* 2016;**16**(7):449–62.
43. Segebarth D, Griebel M, Stein N, von Collenberg CR, Martin C, Fiedler D, Comeras LB, Sah A, Schoeffler V, Luffe T, Durr A, Gupta R, Sasi M, Lillesaar C, Lange MD, Tasan RO, Singewald N, Pape HC, Flath CM, Blum R. On the objectivity, reliability, and validity of deep learning enabled bioimage analyses. *Elife*. 2020;**9**.
44. Phillips D, Schürch CM, Khodadoust MS, Kim YH, Nolan GP, Jiang S. Highly Multiplexed Phenotyping of Immunoregulatory Proteins in the Tumor Microenvironment by CODEX Tissue Imaging. *Frontiers in Immunology.* 2021;**12**:687673.
45. Jarosch S, Kohlen J, Sarker RSJ, Steiger K, Janssen KP, Christians A, Hennig C, Holler E, D'Ippolito E, Busch DH. Multiplexed imaging and automated signal quantification in formalin-fixed paraffin-embedded tissues by ChipCytometry. *Cell Rep Methods.* 2021;**1**(7):100104.
46. Stoltzfus CR, Sivakumar R, Kunz L, Olin Pope BE, Menietti E, Speziale D, Adelfio R, Bacac M, Colombetti S, Perro M, Gerner MY. Multi-Parameter Quantitative Imaging of Tumor Microenvironments Reveals Perivascular Immune Niches Associated With Anti-Tumor Immunity. *Frontiers in immunology.* 2021;**12**:726492.
47. Schürch CM, Bhate SS, Barlow GL, Phillips DJ, Noti L, Zlobec I, Chu P, Black S, Demeter J, McIlwain DR, Kinoshita S, Samusik N, Goltsev Y, Nolan GP. Coordinated Cellular Neighborhoods Orchestrate Antitumoral Immunity at the Colorectal Cancer Invasive Front. *Cell.* 2020;**182**(5):1341–59.e19.
48. Hewitt SM, Baskin DG, Frevert CW, Stahl WL, Rosa-Molinar E. Controls for immunohistochemistry: the Histochemical Society's standards of practice for validation of immunohistochemical assays. *J Histochem Cytochem.* 2014;**62**(10):693–7.
49. Chester C, Maecker HT. Algorithmic Tools for Mining High-Dimensional Cytometry Data. *The Journal of Immunology.* 2015; **195**(3):773–9.
50. Edfors F, Hober A, Linderback K, Maddalo G, Azimi A, Sivertsson A, Tegel H, Hober S, Szigyarto CA, Fagerberg L, von Feilitzen K, Oksvold P, Lindskog C, Forsstrom B, Uhlen M. Enhanced validation of antibodies for research applications. *Nat Commun.* 2018;**9**(1):4130.
51. Sulczewski FB, Maqueda-Alfaro RA, Alcantara-Hernandez M, Perez OA, Saravanan S, Yun TJ, Seong D, Arroyo Hornero R, Raquer-McKay HM, Esteva E, Lanzar ZR, Leylek RA, Adams NM, Das A, Rahman AH, Gottfried-Blackmore A, Reizis B, Idoyaga J. Transitional dendritic cells are distinct from conventional DC2 precursors and mediate proinflammatory antiviral responses. *Nat Immunol.* 2023;**24**(8):1265–80.
52. Girard M, Law JC, Edilova MI, Watts TH. Type I interferons drive the maturation of human DC3s with a distinct costimulatory profile characterized by high GITRL. *Science Immunology.* 2020;**5**(53):eabe0347.
53. Yin X, Yu H, Jin X, Li J, Guo H, Shi Q, Yin Z, Xu Y, Wang X, Liu R, Wang S, Zhang L. Human Blood CD1c+ Dendritic Cells Encompass CD5high and CD5low Subsets That Differ Significantly in Phenotype, *Gene Expression, and Functions. J Immunol.* 2017;**198**(4):1553–64.
54. Villani A-C, Satija R, Reynolds G, Sarkizova S, Shekhar K, Fletcher J, Griesbeck M, Butler A, Zheng S, Lazo S, Jardine L, Dixon D, Stephenson E, Nilsson E, Grundberg I, McDonald D, Filby A, Li W, De Jager PL, Rozenblatt-Rosen O, Lane AA, Haniffa M, Regev A, Hacohen N. Single-cell RNA-seq reveals new types of human blood dendritic cells, monocytes, and progenitors. *Science (New York, NY)*. 2017;**356**(6335).
55. See P, Dutertre C-A, Chen J, Günther P, McGovern N, Irac SE, Gunawan M, Beyer M, Händler K, Duan K, Sumatoh HRB, Ruffin N, Jouve M, Gea-Mallorquí E, Hennekam RCM, Lim T, Yip CC, Wen M, Malleret B, Low I, Shadan NB, Fen CFS, Tay A, Lum J, Zolezzi F, Larbi A, Poidinger M, Chan JKY, Chen Q, Renia L, Haniffa M, Benaroch P, Schlitzer A, Schultze JL, Newell EW, Ginhoux F. Mapping the human DC lineage through the integration of high-dimensional techniques. *Science (New York, NY)*. 2017;**356**(6342):eaag3009.
56. Pasqual G, Chudnovskiy A, Tas JMJ, Agudelo M, Schweitzer LD, Cui A, Hacohen N, Victora GD. Monitoring T cell-dendritic cell interactions in vivo by intercellular enzymatic labelling. *Nature Publishing Group.* 2018;**553**(7689):496–500.

https://doi.org/10.1017/S2633903X24000138 Published online by Cambridge University Press

57. Leylek R, Alcántara-Hernández M, Lanzar Z, Lüdtke A, Perez OA, Reizis B, Idoyaga J. Integrated Cross-Species Analysis Identifies a Conserved Transitional Dendritic Cell Population. *Cell reports.* 2019;**29**(11):3736–50.e8.
58. Wood GS, Freudenthal PS. CD5 monoclonal antibodies react with human peripheral blood dendritic cells. *The American journal of pathology.* 1992;**141**(4):789–95.
59. Cattoretti G, Büttner M, Shaknovich R, Kremmer E, Alobeid B, Niedobitek G. Nuclear and cytoplasmic AID in extrafollicular and germinal center B cells. *Blood.* 2006;**107**(10):3967–75.
60. Willenbrock K, Renné C, Rottenkolber M, Klapper W, Dreyling M, Engelhard M, Küppers R, Hansmann M-L, Jungnickel B. The expression of activation induced cytidine deaminase in follicular lymphoma is independent of prognosis and stage. *Histopathology.* 2009;**54**(4):509–12.
61. Ehrhardt GRA, Hijikata A, Kitamura H, Ohara O, Wang J-Y, Cooper MD. Discriminating gene expression profiles of memory B cell subpopulations. *The Journal of experimental medicine.* 2008;**205**(8):1807–17.
62. Kang Z, Szabo A, Farago T, Perez-Villatoro F, Launonen I-M, Anttila E, Elias K, Casado J, Sorger P, Färkkilä A. Tribus: Semi-automated discovery of cell identities and phenotypes from multiplexed imaging and proteomic data. 2024.
63. Holman DR, Rubin SJS, Ferenc M, Holman EA, Koron AN, Daniel R, Boland BS, Nolan GP, Chang JT, Rogalla S. Automated spatial omics landscape analysis approach reveals novel tissue architectures in ulcerative colitis. *Sci Rep.* 2024;**14**(1):18934.
64. Wang K, Yang Y, Wu F, Song B, Wang X, Wang T. Comparative analysis of dimension reduction methods for cytometry by time-of-flight data. *Nat Commun.* 2023;**14**(1):1836.
65. Amir E-aD, Davis KL, Tadmor MD, Simonds EF, Levine JH, Bendall SC, Shenfeld DK, Krishnaswamy S, Nolan GP, Pe'er D. viSNE enables visualization of high dimensional single-cell data and reveals phenotypic heterogeneity of leukemia. *Nature Biotechnology.* 2013;**31**(6):545– 52.
66. Geuenich MJ, Hou J, Lee S, Ayub S, Jackson HW, Campbell KR. Automated assignment of cell identity from single-cell multiplexed imaging and proteomic data. *Cell systems.* 2021;**12**(12):1173–86.e5.

Cite this article: Bolognesi MM, Dall'Olio L, Maerten A, Borghesi S, Castellani G & Cattoretti G (2024). Seeing or believing in hyperplexed spatial proteomics via antibodies: New and old biases for an image-based technology. *Biological Imaging*, 4: e10. doi: https://doi.org/10.1017/S2633903X24000138